Molecular Systems Biology (2005) doi:10.1038/msb4100032

www.molecularsystemsbiology.com

molecular systems biology

REPORT

Monitoring dynamics of single-cell gene expression over multiple cell cycles

Scott Cookson[1,3], Natalie Ostroff[1,3], Wyming Lee Pang[1,3], Dmitri Volfson[1,2] and Jeff Hasty[1,*]

[1] Department of Bioengineering, University of California at San Diego, La Jolla, CA, USA and [2] Institute for Nonlinear Science, University of California at San Diego, La Jolla, CA, USA
[3] These authors contributed equally to this work
* Corresponding author. Department of Bioengineering, University of California at San Diego, 9500 Gilman Drive, La Jolla, CA 92093-0412, USA.
Tel.: +1 858 822 3442; Fax: +1 309 273 0130; E-mail: hasty@ucsd.edu

Received 11.7.05; accepted 27.10.05

Recent progress in reconstructing gene regulatory networks has established a framework for a quantitative description of the dynamics of many important cellular processes. Such a description will require novel experimental techniques that enable the generation of time-series data for the governing regulatory proteins in a large number of individual living cells. Here, we utilize microfabrication to construct a Tesla microchemostat that permits single-cell fluorescence imaging of gene expression over many cellular generations. The device is used to capture and constrain asymmetrically dividing or motile cells within a trapping region and to deliver nutrients and regulate the cellular population within this region. We illustrate the operation of the microchemostat with *Saccharomyces cerevisiae* and explore the evolution of single-cell gene expression and cycle time as a function of generation. Our findings highlight the importance of novel assays for quantifying the dynamics of gene expression and cellular growth, and establish a methodology for exploring the effects of gene expression on long-term processes such as cellular aging.
Molecular Systems Biology 22 November 2005; doi:10.1038/msb4100032
Subject Categories: functional genomics; synthetic biology
Keywords: gene regulation; microfluidics; microscopy

Introduction

Systems biology has grown rapidly in the wake of the human genome project, as it has become clear that an integration of experimental and computational research will be required to quantitatively describe complex biological systems. The utilization of high-throughput technologies has led to the successful reconstruction of gene regulatory networks in many organisms (Tavazoie *et al*, 1999; Ideker *et al*, 2001; Ibarra *et al*, 2002; Gardner *et al*, 2003), along with the development of quantitative models for many complex and fundamental cellular processes (Vogelstein *et al*, 2000; Simon *et al*, 2001; Breeden, 2003; Bartek *et al*, 2004; Begley and Samson, 2004; Kohn and Pommier, 2005). To complement the progress of genome-scale measurement technologies, a primary focus of synthetic biology is to model and construct novel genetic circuits that reproduce the behavior of natural systems and contribute to our understanding of how complex biological functions arise from the connectivity of gene regulatory networks (Hasty *et al*, 2002; Mangan *et al*, 2003; Basu *et al*, 2005; Pedraza and v Oudenaarden, 2005; Rosenfeld *et al*, 2005). The significant potential of synthetic biology will rest on the development of new tools both for the acquisition and processing of data from large samples of individual cells (Thompson *et al*, 2004; Tourovskaia *et al*, 2005), which will facilitate the characterization of both native and synthetic biological systems. The utility of single-cell measurements with high temporal resolution has been demonstrated by recent bacterial studies, which used optical microscopy to observe *Escherichia coli* over long time periods and reveal interesting temporal fluctuations and cell–cell variability that would otherwise be masked by population-wide measurements (Pedraza and v Oudenaarden, 2005; Rosenfeld *et al*, 2005). However, traditional microscopy methods, which typically involve viewing cells on a microscope slide or an agar plate, limit both the length and quality of an experimental run, as large groups of cells tend to grow out of the focal plane.

Microfabrication (Duffy *et al*, 1999; Hansen and Quake, 2003) can be used to construct custom microfluidic devices in which cells can be cultured in a tightly regulated microenvironment (Balagaddé *et al*, 2005; Groisman *et al*, 2005). Here, we present the development and application of a 'free-running' microfluidic platform tailored to the generation and analysis of single-cell fluorescence data over many cellular generations. We demonstrate the utility of the platform with experimental data acquired from *Saccharomyces cerevisiae*, a workhorse for eukaryotic cell biology. In addition, we present software designed for the extraction of time-series data from a sequence

of fluorescence images. The availability of this device should greatly aid quantitative modelers of both native and synthetic genetic circuits by facilitating the long-term observance of dynamical properties of gene regulation in *S. cerevisiae* and other model organisms.

Results and discussion

The Tesla microchemostat (TμC) is based on an implementation of the classic Tesla diode loop (Tesla 1920; Duffy *et al*, 1999; Bendib and Français, 2001), modified for the imaging of a monolayer culture of cells growing in exponential phase for many generations. The construction is such that the side-arm of the diode forms a shallow trapping region that constrains a population of cells to the same focal plane (Figure 1). Fluid flow is utilized to continuously purge cells that grow beyond the trapping region boundaries so that the device can function as a standard chemostat. Coupled with optical autofocus, this design feature allows for the TμC to operate in 'free-run' mode over long time periods without the need for external adjustment.

In order to achieve free-running long experimental runs, a critical design objective was to avoid clogging between the media port and the trapping region. We developed a three-port chip design in which the main channel extending from the cell port splits into both a media channel and a waste channel downstream of the trapping region, which prohibits the collection of cells in the media port during the loading process (Figure 1A). By constructing the height of the bypass channel to be two or three times the height of the trapping region, substantial flow can be maintained throughout this channel while flow through the trapping region remains minimal. Once cells are loaded, they receive nutrients via a combination of diffusion and advection. As the colony grows, fluidic resistance increases through the trapping region, and diffusion dominates the transport process (see Supplementary information for a detailed analysis of nutrient transport). Supplied with abundant nutrients, the cells are able to grow exponentially to fill the trapping region in a monolayer (Figures 1C and D). The open walls of the trapping region allow for peripheral cells to escape when they are pushed into the high flow of the main channel, thus permitting continuous exponential growth long after the trapping region becomes full.

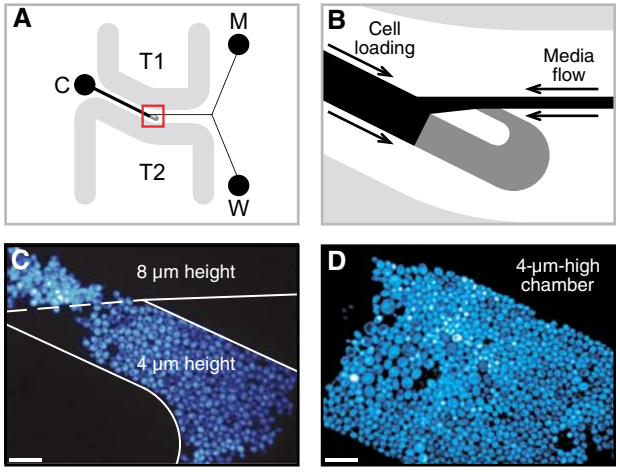

Figure 1 The TμC design was optimized to allow for long-term growth of cells in a monolayer. (**A**) Three separate ports for cell loading (C), media supply (M), and waste (W) minimize potential clogging of media supply lines. With this layout, we are able to generate optimal fluid flow both for the loading of cells into the trapping region and for the delivery of nutrients over many generations. Strong flow toward the trapping region provides the momentum necessary to carry cells into the region against high resistance. Cells that do not enter the trapping region are forced into the waste port by strong flow from the media port. Once cells are loaded, flow is reversed to run from the media port to both the waste and cell ports. Running temperature-regulated water through thermal lines T1 and T2 maintains the device at an optimal temperature. (**B**) A zoomed-in view of the diode loop. The height of the trapping region (dark gray) is customized based on species. The flow channels (black) are 2–3 times higher than the trapping region. An open trapping region (black/gray interface) allows for peripheral cells to be pushed from the observation region as the colony grows. (**C**) Shallow trapping regions confine cells to a monolayer. Cells residing at the trapping region entrance highlight the benefit of a height-constrained growth environment. Scale bar, 20 μm. (**D**) The 4-μm-high yeast TμC full of cells after 24 h of growth. Scale bar, 20 μm.

Based on these design considerations, the TμC is constructed using well-documented microfabrication techniques (see Materials and methods). Briefly, a poly(dimethylsiloxane) (PDMS) chip is created with the desired channels and microstructures from a patterned silicon wafer template. Device fabrication is relatively straightforward, as it requires only a single PDMS layer. Furthermore, flow control is maintained by passive gravitational forces alone, eliminating the need for complex on-chip actuators, flow circuitry, and run-time software. The minimal three-port design allows for a rapid experimental setup that has been optimized for convenience and requires approximately 1 h of bench time. The simplicity of device construction and experimental setup makes the platform accessible to experimentalists with minimal experience in microfabrication.

We illustrate the utility of the device using the budding yeast *S. cerevisiae,* an excellent test for the TμC device owing to the tendency of cells to flocculate, or aggregate into clumps. This property presents a major obstacle in the attainment of long-term single-cell temporal data in this important model organism (Hartwell *et al*, 1997; Simon *et al*, 2001; Simon and Yen, 2003; Chen *et al*, 2004; McMurray and Gottschling, 2004; Scheibel *et al*, 2004). To address this problem, we designed the trapping region height to be approximately equal to the diameter of a single yeast cell. The significant advantage of monolayer growth in a height-constrained chamber is demonstrated by visualizing the group of cells residing at the trapping region boundary (Figure 1C). The cells growing inside the 4-μm-high cell chamber are collectively in focus, and individual cells can easily be distinguished. In contrast, cells just outside of the chamber, where the height is 8 μm, grow in multiple layers, producing blurry aggregates from which quantitative single-cell data are very difficult to extract using wide-field microscopy. Although this may not impede the observation of a few cells over a short period of time, as these cells begin to divide it becomes increasingly difficult to resolve individual cells and quantify their behavior.

Using the TμC device to grow a monolayer colony of cells, we can obtain a long sequence of consistently focused fluorescence images (see Supplementary Movie 1). The extraction of single-cell expression dynamics from a sequence of images involves two major steps: (i) we segment each image into individual cells and (ii) we resolve the temporal evolution from the segmented images (see Supplementary information

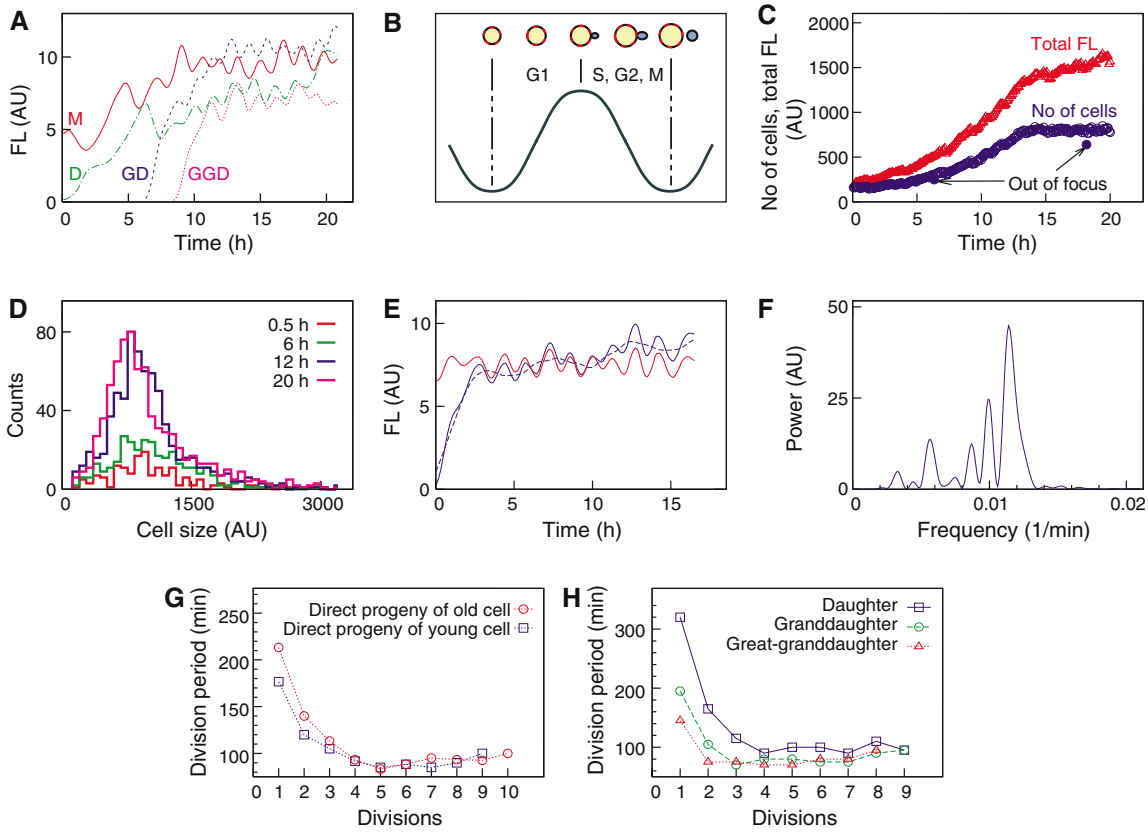

Figure 2 (**A**) Four representative, directly related (mother, daughter, granddaughter, great-granddaughter) trajectories showing fluorescence of each cell as a function of time. (**B**) Cartoon illustrating how the cell tracking leads to oscillations in a gene expression time series. (**C**) Total number of segmented cells as a function of time and the sum of the fluorescent signals of all cells as a function of time. (**D**) Histograms of cell sizes at various times throughout the experiment. (**E**) Data processing: raw data smoothed with an 8-point Savitsky–Golay filter (solid blue line); long-term trend obtained with a 45-point Savitsky–Golay filter (dashed blue); detrended data input to Lomb–Scargle transform (solid red). (**F**) Sample frequency spectrum of a typical trajectory, where the 0.0116 1/min frequency peak corresponds to a cell division period of 86.1 min. (**G**) The time per division versus division number for progeny of a nearly senescent cell and progeny of a younger cell. Each curve is averaged over three cells. (**H**) The time per division versus division number for the daughter, granddaughter, and great-granddaughter of a nearly senescent cell.

and Supplementary Movie 3). We utilized cells that exhibit galactose-dependent expression of yeast-enhanced Venus fluorescent protein (yEVFP) from three integrated copies of the *GAL1* promoter driving yEVFP. Fully induced cells are tracked through a series of images, yielding fluorescence trajectories that rise and fall with each cell cycle (Figures 2A and 3). Since segmentation involves tracking a daughter cell from the moment the bud begins to emerge, the fluorescence signal of the mother is observed to decrease as yEVFP freely diffuses to the bud throughout the S, G2, and M phases. The fluorescence signal rises again at the beginning of the next G1 phase, when the mother and daughter have fully divided and the mother can resume the accumulation of fluorescent protein (Figure 2B). The cell count grows exponentially until the chamber fills, at which point the chemostat enables extended run-times as the population can continue growing by pushing peripheral cells out of the trapping region (Figure 2C). Histograms of cell sizes at different time points throughout the experiment retain a constant distribution, indicating that growth conditions remain optimal for the duration of the run (Figure 2D).

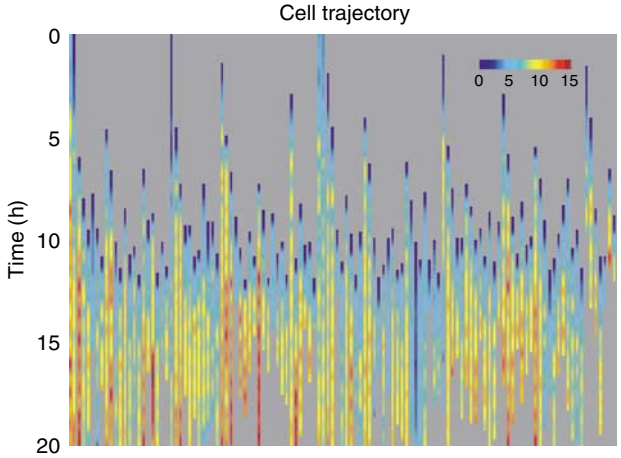

Figure 3 Single-cell yellow fluorescent protein (YFP) dynamics for 119 cells. Each column corresponds to a density plot that depicts the evolution of the amount of YFP in a single cell over a period of many hours (the scale bar denotes arbitrary units consistent with Figure 2). Variations in cycle times and long-term trends are clearly discerned. The dynamics of YFP production and division were generated from the cells shown in Supplementary Movie 1.

The most novel utility of the TμC is the ability to observe single-cell dynamics over long time periods. Quantitative accuracy of the fluorescence trajectories can be ensured by compensating for errors that may be introduced by experimental conditions and image analysis (see Supplementary information). These trajectories can be used to extract many types of information about individual cells, such as the average cell cycle time for any individual cell (Figures 2E and F). We can also use fluorescence to monitor how the division rate of an individual cell evolves as it ages. Given that the local minima of a trajectory mark the beginning of each G1 phase, we can calculate the duration of each cell division as the time between each G1 start. As expected, the first cell cycle of a new bud is unusually long, as the bud first has to grow to a certain size before it can begin producing buds of its own. However, our fluorescence data suggest that it often takes a young cell two or three cycles to recover to a normal division rate (Figure 2G). This phenomenon is particularly pronounced in daughters of old, nearly senescent cells, as reported in various studies of aging in yeast (Egilmez and Jazwinski, 1989). Figure 2G compares the evolution of division times for direct progeny of an old cell and direct progeny of a young cell, averaged over three examples of each. For progeny of the young cell, we see that the first division time is long, as expected, and then the cells quickly recover down to a steady division rate. In contrast, progeny of older cells take longer to reach this steady state, as indicated by the longer division times for the first few cell cycles. This phenomenon is highlighted in Figure 2H, where the division times for the daughter, granddaughter, and great-granddaughter of a nearly senescent cell are plotted. We observe that the daughter takes three cycles to recover to steady state, the granddaughter takes two cycles to recover, and the great-granddaughter recovers immediately. These cycle-time results are consistent with previous studies that utilized different assays (Egilmez and Jazwinski, 1989), and the ability to simultaneously track gene expression over long periods highlights the utility of the device.

The ability to perform long-duration experiments that yield consistent single-cell data is critical for the generation of computational models with predictive abilities, a hallmark of synthetic biology. We have demonstrated the utility of a novel microchemostat that can be used for monitoring cellular dynamics over many generations. This device offers a number of significant technical advantages over existing methods such as flow cytometry and traditional microscopy. Flow cytometry provides a snapshot of single-cell data, but does not offer the ability to dynamically track a given single cell. These population measurements provide very useful information about the steady-state behavior of biological networks, but they inherently sacrifice details at the single-cell dynamical level. Traditional microscopy assays yield useful and very detailed information on the dynamical behavior of a small number of cells but typically run only for a short time period and sacrifice the ability to generate good statistics over a population. In contrast, the TμC we have designed and developed allows for long-term single-cell dynamical measurements over a large population. Within the context of systems biology, the ability to generate such data at the single-cell level will aid in the development of predictive dynamical modeling (Chen *et al*, 2004) and facilitate the application of novel approaches such as the use of frequency-space analysis to quantify the variability inherent in gene expression (Simpson *et al*, 2003). The unique capability of the TμC for studying both the dynamics and the variability of biological processes within a population of living cells represents an important step toward bringing quantitative single-cell data to the field of systems biology.

Materials and methods

Fabrication procedure

Microfluidic devices were constructed using well-established techniques (Duffy *et al*, 1999; Hansen and Quake, 2003) and the UCSD Integrated Technology Lab (ITL). Briefly, photolithographic photomasks were drawn using FreeHand MX (Macromedia Inc., San Francisco, CA), printed onto transparency film at high resolution (Output City, Poway, CA), and mounted to clean borosilicate glass plates (McMaster-Carr, Los Angeles, CA). To make master molds, SU-8 2000 (MicroChem Corp., Newton, MA) was spin coated to appropriate depths using a Headway PWM32 programmable spinner (Headway Research Inc., Garland, TX) and patterned by UV exposure via appropriate photomasks using a contact mask aligner (HTG, San Jose, CA). After all photolithographic steps were completed, SU-8 feature heights were verified using a DEKTAK 3030ST profilometer (Sloan Technology Corp., Santa Barbara, CA), and treated with vaporous chlorotrimethylsilane for 5–10 min. PDMS/Sylgard 184 (Dow Corning, Midland, MI) was mixed in a 10:1 ratio with the supplied crosslinking agent and degassed in a vacuum desiccator at −15 mmHg for 30 min to 1 h. The degassed PDMS was then poured over the silicon/SU-8 master to a depth of approximately 0.5 cm and cured at 80°C for 1 h. After curing, the hardened PDMS monolith was carefully released from the master. Fluidic ports for media/cell loading and heated water lines were bored with 20- and 16-gauge Luer stub adapters, respectively, and flushed with 0.2-μm-filtered dH_2O. Individual chips were sectioned from the PDMS monolith and sonicated in a 0.1% v/v Tween 80 solution for 15 min and rinsed in dH_2O. Scotch 810 office tape was used to remove any remaining particles from the PDMS surface. Finally, each chip was exposed to O_2 plasma for 30 s in a Technics 500-II Plasma Asher and brought into contact with plasma-cleaned 24×40 mm No $1\frac{1}{2}$ coverslips (Corning Inc., Corning, NY), which forms a strong irreversible bond between the two surfaces (Wu *et al*, 2002). Our photomask files are freely available for academic use and may be downloaded from our website (http://biodynamics.ucsd.edu/download.html).

Loading procedure

In preparation for cell observation, devices were mounted to the microscope stage and connected to thermal water baths to maintain the optimal growth temperature of 30°C. Thermal connections were made using Tygon microbore tubing (0.050 in ID, 0.090 in OD) (Cole Parmer, Vernon Hills, IL) connected to chip thermal ports with 16-gauge dispensing needles (McMaster-Carr, Los Angeles, CA). Water temperatures flowing into and out of the device were monitored using in-line thermocouples. Following device priming with filtered dH_2O, an open 10 ml syringe serving as a waste reservoir was filled with media and suspended 5 in above the device. A similar media connection was made at the device media port at a height of 25 in. Cells and 2.5-μm-diameter YG fluorescent beads were loaded into the device at the cell port, with the beads serving as a fluorescence intensity standard, until several of each entered the trapping region. During loading, all flows were directed toward the waste port to prevent contamination of the media line. To minimize clogging, strong flow from the media port was used to flush clear all cells residing in the shared fluid channels. Finally, the three reservoirs were brought to their final run-time heights, with the cell reservoir fixed at a height 1 in above the waste reservoir and the media reservoir fixed at a height 1 in above the cell reservoir. These differential heights provided for

both gentle flow of media through the trapping region and strong flow of media into the waste port, thereby feeding the cells to be monitored while preventing discarded cells from re-entering the system.

Strain and cell culture

The yeast strain was created by targeted chromosomal integration of the pRS61-yv vector at the Gal1-10 locus of *S. cerevisiae* strain K699 (a, ADE2, ura3, his3, trp1, leu2). The vector was constructed using standard recombination techniques from two commercially available vectors: the tryptophan marker from pRS404 was inserted into the pESC-His vector, which contains the Gal1-10 promoter locus of *S. cerevisiae* (see Supplementary Figure S8). yEVFP, a yellow fluorescent protein (YFP) variant, was inserted behind the Gal1 promoter for fluorescence production inducible by the addition of galactose to the medium. Cultures were grown in synthetic drop-out (SD) medium supplemented with all amino acids except histidine for selection of the correct integrant and containing 2% glucose. After selection, cultures were grown in SD supplemented with all amino acids and containing 2% galactose for full induction of the production of the yEVFP. To minimize flocculation of yeast while growing in the incubator shaker, single colonies were initially inoculated into 1 ml of medium in a microcentrifuge tube and vortexed on high for 2 min before being transferred to a culture tube with 4 ml total medium. Cultures were then grown at 30°C for 18–24 h to an OD_{600} of 1.0 ± 0.25. In preparation for loading, four samples from a single culture were diluted into 1 ml of medium in a microcentrifuge tube to an OD_{600} of 0.05 and vortexed for 5–10 min. Cultures were then combined with 4 ml of total culture for loading into the chip.

Data acquisition

Image acquisition was performed on a Nikon Diaphot TMD epifluorescent inverted microscope outfitted with fluorescence excitation and emission filter wheels, an XY motorized stage and fine focus motor with a hardware-based autofocus controller (Prior Scientific, Rockland, MA), and Uniblitz VS35 high-speed shutters (Vincent Associates, Rochester, NY) mounted in the fluorescence and transmitted light paths. Images were acquired using a Hamamatsu ORCA-ERG cooled CCD camera and a custom positioning and multispectral acquisition application written in LabVIEW (National Instruments, Austin, TX). Imaging for the autofocus controller was performed using a COHU 4900 series CCTV camera mounted to one of the microscope eyepieces. Fluorescence visualization was performed with narrow band-pass excitation and emission filters for RFP and YFP (Chroma Inc., Rockingham, VT) for beads and yEVFP, respectively.

Supplementary information

Supplementary information is available at the *Molecular Systems Biology* website (www.nature.com/msb).

Acknowledgements

We thank Dmitri Bratsun for design suggestions based on the Tesla diode, Ting Lu for assistance in analyzing the flow properties of the diode, and Alex Groisman for technical advice on microfabrication. This work was supported by the NSF Division of Cellular and Molecular Bioscience, the Alfred P Sloan Foundation (JH), the DOE CSGF (NO), and the DOD NDSEG Fellowship Program (SC).

References

Balagaddé FK, You L, Hansen CL, Arnold FH, Quake SR (2005) Long-term monitoring of bacteria undergoing programmed population control in a microchemostat. *Science* **309:** 137–140

BarteK J, Lukas C, Lukas J (2004) Checking on DNA damage in S phase. *Nat Rev Mol Cell Biol* **5:** 792–804

Basu S, Gerchman Y, Collins CH, Arnold FH, Weiss R (2005) A synthetic multicellular system for programmed pattern formation. *Nature* **434:** 1130–1134

Begley TJ, Samson LD (2004) Network responses to DNA damaging agents. *DNA Repair (Amst)* **3:** 1123–1132

Bendib S, Français O (2001) Analytical study of microchannel and passive microvalve 'application to micropump simulator'. In *Design, Characterisation, and Packaging for MEMS and Microelectronics 2001*, Adelaide, Australia, pp 283–291

Breeden LL (2003) Periodic transcription: a cycle within a cycle. *Curr Biol* **13:** R31–R38

Chen KC, Calzone L, Csikasz-Nagy A, Cross FR, Novak B, Tyson JJ (2004) Integrative analysis of cell cycle control in budding yeast. *Mol Biol Cell* **15:** 3841–3862

Duffy DC, Schueller OJA, Brittain ST, Whitesides GM (1999) Rapid prototyping of microfluidic switches in poly(dimethyl siloxane) and their actuation by electro-osmotic flow. *J Micromech Microeng* **9:** 211–217

Egilmez NK, Jazwinski SM (1989) Evidence for the involvement of a cytoplasmic factor in the aging of the yeast *Saccharomyces cerevisiae*. *J Bacteriol* **171:** 37–42

Gardner TS, D Bernardo D, Lorenz D, Collins JJ (2003) Inferring genetic networks and identifying compound mode of action via expression profiling. *Science* **301:** 102–105

Groisman A, Lobo C, Cho H, Campbell JK, Dufour YS, Stevens AM, Levchenko A (2005) A microfluidic chemostat for experiments with bacterial and yeast cells. *Nat Methods* **2:** 685–689

Hansen C, Quake SR (2003) Microfluidics in structural biology: smaller, faster …better. *Curr Opin Struct Biol* **13:** 538–544

Hartwell LH, Szankasi P, Roberts CJ, Murray AW, Friend SH (1997) Integrating genetic approaches into the discovery of anticancer drugs. *Science* **278:** 1064–1068

Hasty J, McMillen D, Collins JJ (2002) Engineered gene circuits. *Nature* **420:** 224–230

Ibarra RU, Edwards JS, Palsson BO (2002) *Escherichia coli* K-12 undergoes adaptive evolution to achieve *in silico* predicted optimal growth. *Nature* **420:** 186–189

Ideker T, Thorsson V, Ranish JA, Christmas R, Buhler J, Eng JK, Bumgarner R, Goodlett DR, Aebersold R, Hood L (2001) Integrated genomic and proteomic analyses of a systematically perturbed metabolic network. *Science* **292:** 929–934

Kohn KW, Pommier Y (2005) Molecular interaction map of the p53 and Mdm2 logic elements, which control the Off–On switch of p53 in response to DNA damage. *Biochem Biophys Res Commun* **331:** 816–827

Mangan S, Zaslaver A, Alon U (2003) The coherent feedforward loop serves as a sign-sensitive delay element in transcription networks. *J Mol Biol* **334:** 197–204

Mcmurray MA, Gottschling DE (2004) Aging and genetic instability in yeast. *Curr Opin Microbiol* **7:** 673–679

Pedraza JM, v Oudenaarden A (2005) Noise propagation in gene networks. *Science* **307:** 1965–1969

Rosenfeld N, Young JW, Alon U, Swain PS, Elowitz MB (2005) Gene regulation at the single-cell level. *Science* **307:** 1962–1965

Scheibel T, Bloom J, Lindquist SL (2004) The elongation of yeast prion fibers involves separable steps of association and conversion. *Proc Natl Acad Sci USA* **101:** 2287–2292

Simon I, Barnett J, Hannett N, Harbison CT, Rinaldi NJ, Volkert TL, Wyrick JJ, Zeitlinger J, Gifford DK, Jaakkola TS, Young RA (2001) Serial regulation of transcriptional regulators in the yeast cell cycle. *Cell* **106:** 697–708

Simon JA, Yen TJ (2003) Novel approaches to screen for anticancer drugs using *Saccharomyces cerevisiae*. *Methods Mol Biol* **223:** 555–576

Simpson ML, Cox CD, Sayler GS (2003) Frequency domain analysis of noise in autoregulated gene circuits. *Proc Natl Acad Sci USA* **100:** 4551–4556

Tavazoie S, Hughes JD, Campbell MJ, Cho RJ, Church GM (1999) Systematic determination of genetic network architecture. *Nat Genet* **22:** 281–285

Tesla N (1920) US patent no. 1,329,559, 03 February 1920

Thompson DM, King KR, Wieder KJ, Toner M, Yarmush ML, Ja-Yaraman A (2004) Dynamic gene expression profiling using a microfabricated living cell array. *Anal Chem* **76:** 4098–4103

Tourovskaia A, Figueroa-Masot X, Folch A (2005) Differentiation-on-a-chip: a microfluidic platform for long-term cell culture studies. *Lab Chip* **5:** 14–19

Vogelstein B, Lane D, Levine AJ (2000) Surfing the p53 network. *Nature* **408:** 307–310

Wu ZY, Xanthopoulos N, Reymond F, Rossier JS, Girault HH (2002) Polymer microchips bonded by O_2-plasma activation. *Electrophoresis* **23:** 782–790

Monitoring dynamics of single-cell gene expression over multiple cell cycles

Supplementary Information

Scott Cookson[1,†], Natalie Ostroff[1,†], Wyming Lee Pang[1,†], Dmitri Volfson[1,2] & Jeff Hasty[1,*]

[1] Department of Bioengineering, University of California San Diego, La Jolla, CA 92093
[2] Institute for Nonlinear Science, University of California San Diego, La Jolla, CA 92093
[†]These authors contributed equally to this work.
[*]Corresponding author.

Nutrient transport within the TμC

We used two methods to characterize fluid flow through the TμC under typical run-time conditions. First, we used 0.5 μm yellow-green beads as tracers to map the flow field through the trapping region under the pressures used to deliver nutrients. We acquired a movie of bead flow at 10 frames per second and used this as input to a MATLAB implementation of the Particle Image Velocimetry (PIV) method [1]. PIV provides a vector field that accurately describes the magnitude and direction of flow, and the results affirmed our prediction of creeping flow through the trapping region (Figure S1). From this vector field, the maximum velocity through the feeder channel was found to be 75 μm/s and the mean velocity through the trapping region was 1.5 μm/s.

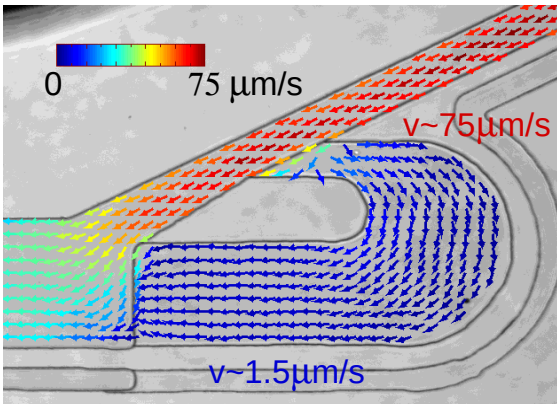

Figure S1: A Particle Image Velocimetry method analyzes images of fluorescent beads used as flow tracers. The result is the vector field shown here, where the direction of flow is given by arrowheads and the magnitude is given by the color of the arrow (on a log scale).

In order to ensure that a culture growing in the trapping region would receive sufficient nutrients, we performed a more detailed flow characterization by simulating nutrient delivery using two red fluorescent dyes. Nutrient transport throughout the trapping region of the TμC is driven by both advective and diffusive processes, and the key parameters involved in the process are the diffusion coefficient of each nutrient species and the advective velocity through the trapping region. We modeled the transport process by deriving a closed form solution of the time dependent chemical concentration profile throughout the trapping region. The analytical solution was fit to experimental data, yielding an estimate of the advective velocity.

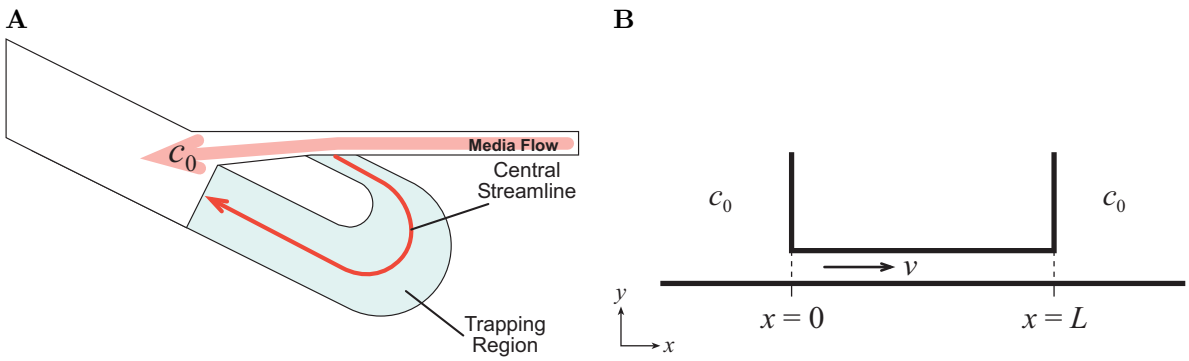

Figure S2: (**A**) Schematic of chamber streamline. (**B**) 1D channel with diffusive and advective transport

The chemical species mass balance for unsteady diffusion with advection is,

$$\frac{\partial c}{\partial t} + \vec{v} \cdot \vec{\nabla} c = \mathcal{D} \nabla^2 c \tag{1}$$

Because flow within the microfluidic device is restricted to the laminar regime, analysis can be performed on the central streamline of flow through the trapping region (Figure S2A). It is assumed that components of the velocity and concentration gradient normal to the direction of flow are negligible relative to the tangent components. Using this assumption, the physical process can be reduced to a 1D system (Figure S2B), simplifying Eqn. 1 to,

$$\frac{\partial c}{\partial t} + V_0 \frac{\partial c}{\partial x} = \mathcal{D} \frac{\partial^2 c}{\partial x^2} \tag{2}$$

with the following boundary and initial conditions,

$$c(0, t) = c_0, \ t > 0 \tag{3}$$

$$c(L, t) = c_0, \ t > 0 \tag{4}$$

$$c(x, 0) = 0, \ 0 < x < L \tag{5}$$

Here V_0 is the average channel velocity, $\mathcal{D}$ is the molecular diffusivity of the chemical species, and c_0 is both the steady-state and boundary supported concentration.

The system of equations can be further simplified by introducing the following dimensionless parameters,

$$C = \frac{c - c_0}{c_0} \qquad \xi = \frac{x}{L} \qquad \tau = \frac{\mathcal{D}}{L^2} t \tag{6}$$

Hence, Eqns. 2-5 become,

$$\frac{\partial C}{\partial \tau} + N_{\mathrm{Pe}} \frac{\partial C}{\partial \xi} = \frac{\partial^2 C}{\partial \xi^2} \tag{7}$$

$$C(0, \tau) = 0, \ \tau > 0 \tag{8}$$

$$C(1, \tau) = 0, \ \tau > 0 \tag{9}$$

$$C(\xi, 0) = -1, \ 0 < \xi < 1 \tag{10}$$

where,

$$N_{\mathrm{Pe}} = \frac{V_0 L}{\mathcal{D}} \tag{11}$$

and is commonly known as the Peclet Number, a dimensionless ratio of advective transport to diffusive transport that arises in heat and mass transfer problems. It is important to note that the system is linear with respect to C, with homogeneous boundary conditions and therefore can be easily solved using the method of separation of variables [2], yielding the closed form solution,

$$C(\xi, \tau) = \exp\left(\frac{N_{\mathrm{Pe}}}{2} \xi\right) \sum_{n=1}^{\infty} A_n \sin(n\pi \, \xi) \exp(-\lambda_n \, \tau) \tag{12}$$

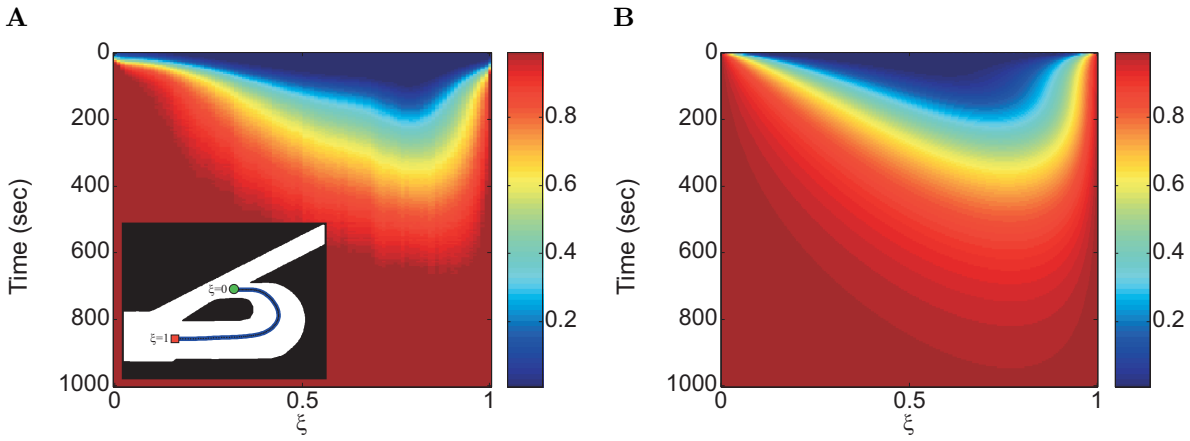

Figure S3: Comparison of experimental data and analytical solution of nutrient transport into the trapping region. (**A**) Experimental data collected using 10 kDa Dextran conjugated Rhodamine B isothiocyanate along the central streamline of the trapping region. The inset shows the path analyzed (blue line) starting from the green circle, and ending at the red square. (**B**) Analytical solution of 1D diffusion with advection for large molecule transport.

or,

$$c(x,t) = c_0 \left\{ \exp\left(\frac{N_{\mathrm{Pe}}}{2L}\, x\right) \sum_{n=1}^{\infty} A_n \sin\left(\frac{n\pi}{L}\, x\right) \exp\left(-\lambda_n \frac{\mathcal{D}}{L^2}\, t\right) + 1 \right\} \tag{13}$$

where,

$$\lambda_n = \frac{1}{4}[(2n\pi)^2 + N_{\mathrm{Pe}}^2] \tag{14}$$

$$A_n = 4 \exp\left(-\frac{N_{\mathrm{Pe}}}{2}\right) \left\{ \frac{2n\pi\, \cos(n\pi) + N_{\mathrm{Pe}}\, \sin(n\pi) - 2n\pi\, \exp\left(\frac{N_{\mathrm{Pe}}}{2}\right)}{N_{\mathrm{Pe}}^2 + (2n\pi)^2} \right\} \tag{15}$$

Experimental concentration profiles were visualized using 10 kDa conjugated Rhodamine B isothiocyanate. The diffusion constant of the dye was estimated using the Stokes-Einstein equation for large diffusing particles [3],

$$\mathcal{D}_{AB} = \frac{k_b T}{6\pi \mu_B s_A} \tag{16}$$

where $\mathcal{D}_{AB}$ is the diffusion coefficient of solute A in solvent B, k_b is Boltzmann's constant, T is the ambient temperature, μ_B is the dynamic viscosity of solvent B, and s_A is the molecular Stokes radius of solute A. For dextrans, the value of s_A is determined using a previously reported correlation [4] based on molecular weight

$$s_A = 0.488\,(MW)^{0.437} \tag{17}$$

Using this approximation, $\mathcal{D}_{AB}$ for a 10 kDa dextran was found to be 7.90×10^{-7} cm^2 s^{-1}. The calculated diffusivity of the dye was input to our analytical model of the transport process, which yielded a value of 1 μm/s for the advection velocity, V_0, and a path length, L, of 570 μm (approximately the path length analyzed in the experimental data), altogether providing a N_{Pe} of 7.125.

Experimental data was acquired by imaging fluorescent dye entering the trapping region and recording intensity values along the central streamline. Fluorescence images were acquired every 5 s for 1.4 hrs and post-processed by background subtraction, flat-field correction, and smoothing using a 5 pixel gaussian kernel. A quadratic interpolating spline was fit to 6-10 points manually chosen to define the central streamline and then subdivided into 100 points. For each image, path profiles were generated by recording the mean pixel intensity over a 10 μm line normal to the spline as the fluorescence value at each point. Experimental concentration was assumed to be linearly proportional to fluorescence signal and was normalized by the steady-state value. The temporal evolution profiles of the experimental data and the analytical model for the empty device are shown in Figure S3. Analytical data is plotted as $C'(\xi,t) = C(\xi,t) + 1$ calculated from a 100-term Fourier series. A comparison of the two profiles shows good agreement, supporting the existence of creeping flow on the order of 1 μm/s within the trapping region of the device under normal operating conditions. In addition, the calculated velocity of the creeping flow closely matches the value obtained using the PIV method (1.5 versus 1.0 μm/s). The asymmetry in the concentration profile over ξ is

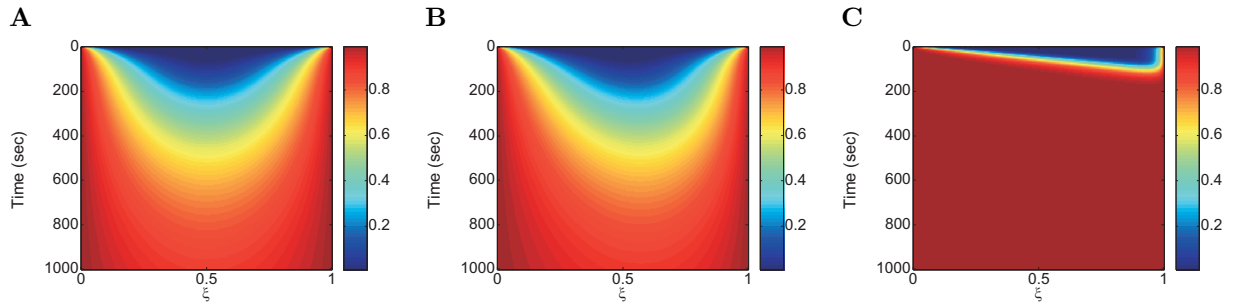

Figure S4: Analytical analysis of the time evolution of 1D concentration profiles for different advective velocities. (**A**) $V_0 = 0$ μm/s, $N_{\mathrm{Pe}} = 0$. (**B**) $V_0 = 0.2$ μm/s, $N_{\mathrm{Pe}} = 1.425$. (**C**) $V_0 = 5$ μm/s, $N_{\mathrm{Pe}} = 36.625$.

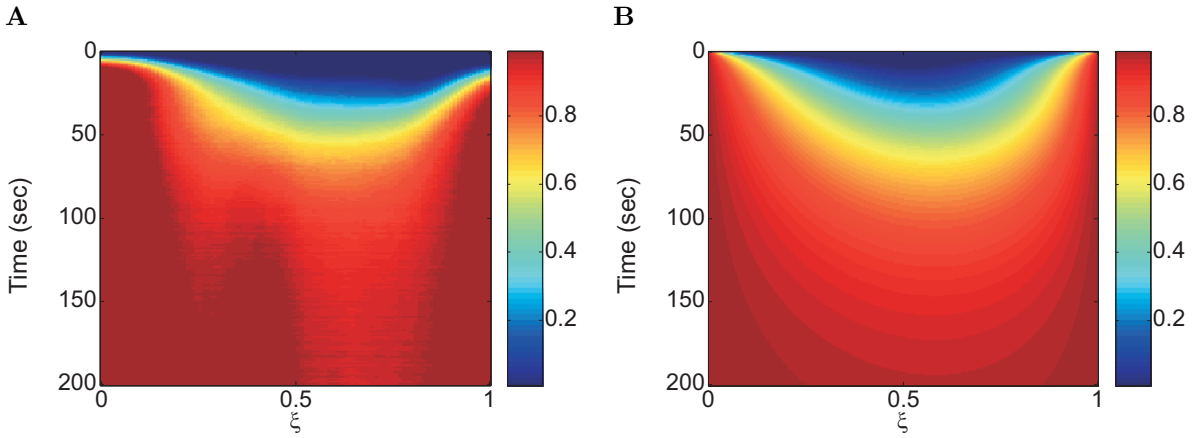

Figure S5: Comparison of experimental data and analytical solution of nutrient transport into the trapping region using Sulphorhodamine 101. (**A**) Experimental data collected along the central streamline of the trapping region. (**B**) Analytical solution of small molecular transport by 1D diffusion with advection.

due primarily to advective transport. Closer inspection of the analytical solution reveals that as $N_{\mathrm{Pe}} \to 0$, Eqns. 12-15 degenerate to the solution for simple 1D unsteady diffusion and the physical process becomes spatially symmetric about $\xi = 0.5$. Moreover, the speed of the transport process is highly dependent on the value of N_{Pe} (Figure S4).

The transport analysis based on the RITC dye provides an estimate for the Peclet Number in the case of a heavy molecule perfusing into the empty trapping region. To better approximate the diffusive transport of nutrients through the trapping region, we used the red dye Sulphorhodamine 101 (Acid Free Texas Red), which has a diffusion constant on the same order of magnitude as a typical nutrient molecule (calculated to be 5.72×10^{-6} cm^2 s^{-1}). Using this smaller dye, experimental and analytical data were analyzed as before (Figure S5). With the diffusion constant an order of magnitude larger than RITC, the Peclet Number will be an order of magnitude smaller, and we expect to see an increased domination of diffusive over advective transport. As cells begin to fill the trapping region, we expect to see the Peclet Number decrease even further, as advective velocity will be slowed by the increased resistance due to the presence of cells. Indeed, upon monitoring Sulphorhodamine dye penetration with the chamber both empty and full of cells, we found that diffusion dominates the transport process (see Supplementary movie 2).

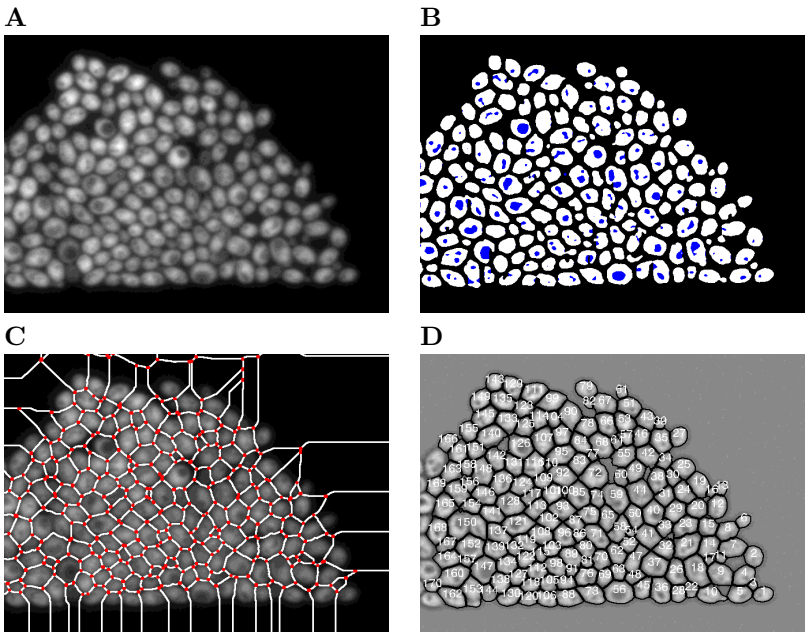

Figure S6: Major steps of image segmentation. For visual clarity, only 1/4 of the whole image is shown. (**A**) Original fluorescent image after flat-field correction and the removal of high-frequency noise. (**B**) Results of initial seeding (white) along with filled "holes" (blue) form the resulting binary mask. (**C**) Results of the watershed segmentation (white lines), segments joining the nodes (red dots) may be eliminated in the interactive mode which allows to merge neighboring cells if needed. (**D**) As a final result of the segmentation, recognized cells are enumerated and their boundaries are shown in black. Cells crossing the boundaries of the field-of-view were abandoned.

Image segmentation software

The extraction of single-cell expression dynamics from a sequence of images involves two major steps: (i) we segment each image into individual cells, and (ii) we resolve the temporal evolution from the segmented images. First, each image is flat-field corrected and pre-processed with a 3×3 Gaussian filter to remove high-frequency noise (Figure S6A). Approximate locations of the cells are determined using a seeding technique [5]. To form seeds, we use the differential of the image averaged with boxcar filters of small and large sizes, 5×5 and 15×15, respectively, which allow for robust location of local maxima of intensity, independent of the mean level of the signal. The resulting binary mask is oversegmented in most cases due to the presence of vacuoles which appear as islands of the background inside the foreground cell seeds (Figure S6B). These islands are eliminated by the transferring of closely-connected regions of the background into the foreground. After this correction, the resulting binary image is processed with a morphological distance transform and a watershed segmentation [6]. The last two operations produce a set of dams which separate cell seeds and are typically located at crests of the gray-scale intensity image (Figure S6C). At the final step of the segmentation, the seeds are used for growing the gray-scale region, an operation which involves expanding the area of the cells from the peaks within the seeds down to a specified level above the background. Here, the watershed dams serve to preclude the joining of neighboring cells during the growth process. In addition, the same skeleton of dams is used to allow for an effective means of manual correction, since the removal of a segment of a dam between touching cells usually results in their joining during the growing of the gray-scale region. The resulting algorithm is implemented using the programming language IDL (The Interactive Data Language, Research Systems, Inc., Boulder, Colorado). In automated mode, which is used in most cases (example is shown in Figure S6D), the segmentation of a single image with 800 cells takes about 30 seconds on a standard personal workstation (see Supplementary movie 3). In this mode, we determined that the fraction of errors in segmentation did not exceed 5% of the total number of recognized cells. Segmentation errors arise primarily when dark regions inside a cell take on values close to the background level, causing the software to draw a watershed line through the cell, or when the boundary between two cells is difficult to observe, causing them to be considered a single cell. For the second step of image analysis, which matches cells recognized in a sequence of images, we adopted a set of tools developed in the context of colloidal suspensions and granular materials [7]. These tools implement cluster analysis, and we used the center of mass coordinates and the total fluorescence integrated over the cellular area as our cluster variables. Errors

in this step arise primarily when a clump of cells near the trapping region boundary breaks off and leaves the chamber, causing a shift in the positions of many cells in the chamber. A manual correction option during each step of the image processing makes it possible to correct for errors, and future implementations of the software will include improvements upon these methods. Our image analysis software is freely available for academic use and may be downloaded from our website (http://biodynamics.ucsd.edu/download.html).

Quantitative controls and error compensation

Quantitative accuracy of the fluorescence trajectories can be ensured by compensating for errors that may be introduced by experimental conditions and image analysis. As a quantitative control, we use calibration-standard fluorescent beads of brightness on the order of the average cell brightness. Because these beads are resistant to photobleaching, any variation in intensity from frame to frame will be a measure of deviations due to either focal drift or fluorescent bulb fluctuations. The trajectory of a bead is shown in Figure S7A alongside a typical cell trajectory, and the coefficient of variation of the bead signal was found to be 3.0%. While this low noise level is negligible when analyzing general trends in data, the bead trajectory can be used to compensate for experimental error in studies for which these fluctuations would be more detrimental.

A concern regarding cells being constrained to a shallow chamber is that nutrients may be unevenly distributed leading to varying growth rates throughout the trapping region. To address this question, we divided the field-of-view into subsections and calculated division rate statistics for all cells residing in each area. We can extract the average cell cycle time for any trajectory by computing and analyzing a power spectrum of the time series data. To account for an occasional gap in a trajectory due to a tracking error, we use the Lomb-Scargle transform for unevenly spaced data to compute a power spectrum from which we can obtain the cell division rate. We calculated the average cell division time for groups of cells in each of 6 regions and found a mean and standard deviation of 86.88 and 3.43 minutes respectively (Figure S7B). This low variation reflects the constant micro-environment throughout the observed region.

Another typical concern in fluorescence microscopy is that the intermittent exposure of fluorescent molecules to high-intensity light will bleach them over time, adversely affecting the data. To address this, we have acquired a photobleaching curve and modeled the effects of exposure on the quantitative integrity of our fluorescence trajectories. In a typical experiment, fluorescence images were acquired every five minutes with exposure times of 50 - 250 ms. With these acquisition settings, effects of photobleaching of yEYFP molecules were determined to be negligible. A photobleaching curve was obtained by subjecting a full field of view of cells expressing yEYFP to constant exposure of fluorescent light. An image was taken every 1.6 seconds and mean fluorescence over a region of interest was plotted against time (Figure S7C). We fit this data using both one and two-exponential functions and for simplicity used a one-exponential fit to obtain the decay rate, γ_p, for yEYFP due to exposure to fluorescent light.

To model the effect of photobleaching on our acquisition of a single-cell fluorescence trajectory, we assume that the fluorescence data obtained from a cell is a combination of the true fluorescence signal, $f(x,t)$, plus a degradation term dependent on the amount of yEYFP present in the cell:

$$\dot{x} = f(x,t) - \gamma_p x \tag{18}$$

In order to extract the true signal, $f(x,t)$, from the observed signal, we use an explicit first order discrete model of the ODE as follows:

$$(x_{i+1} - x_i)\frac{1}{\Delta t} = f_i(x,t) - \gamma_{eff} x_i \tag{19}$$

Here, δt is the time between exposures and is the effective decay rate representing the effect of photobleaching due to a single exposure spread over . This equation can be rearranged to give an expression for $f(x,t)$:

$$f_i = (x_{i+1} - x_i)\frac{1}{\Delta t} + \gamma_{eff} x_i \tag{20}$$

We now want to approximate the actual value of the fluorescence data, $\dot{x} = f$, as it would be recorded if there were no degradation due to photobleaching. The corrected fluorescence value, $\tilde{x}_{i+1}$, at each time point can be evaluated based on the current and previous data points as follows:

$$\tilde{x}_{i+1} = x_i + \Delta t\ f = x_i + \Delta t((x_{i+1} - x_i)\frac{1}{\Delta t} + \gamma_{eff} x_i) = x_{i+1} + \Delta t \gamma_{eff} x_i \tag{21}$$

The effective decay rate, γ_{eff}, should have the same effect on fluorescent intensity over Δt that the calculated decay rate, γ_p, has over the duration of exposure, t_{exp}. That is: $\gamma_{eff}\Delta t = \gamma_p t_{exp}$. Given a maximum exposure time of 250 ms and the value of γ_p calculated from the photobleaching curve of 0.256, we find that the value of $\gamma_{eff}\Delta t$ yields a negligible correction term of 0.1% for each fluorescence value, x_{i+1}. Correcting a given trajectory for this effect has a negligible effect on the data.

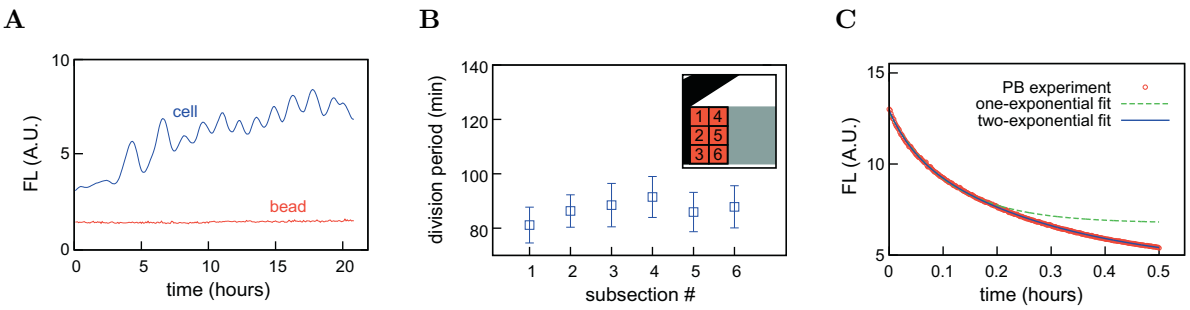

Figure S7: (**A**) The fluorescence trajectory of a bead (red) alongside a sample cell trajectory (blue). (**A**) Mean and standard deviation (error bars) of division rate in each of 6 subsections of the field-of-view. Inset shows a map of subsection. (**C**) Photobleaching experiment. Experimental data is shown by symbols. The best fit is given by a two-exponential function (solid, blue curve). For simplicity, in the analysis we used a single exponential fit (shown by dashed, green curve).

An additional concern regarding the extraction of quantitative information from fluorescence microscopy data is that an individual cell, which often moves throughout the field-of-view due to the growth of neighboring cells, may not experience spatially constant illumination. To address this concern, we applied a flat-field correction to each image, by first filling the field of view with a fluorescent dye of even thickness and acquiring an image at the run-time settings. Assuming that the ideal signal would be constant over all pixels, this image can be used as a weighting template to remove optical artifacts from our data due to variations in either the pixel-to-pixel sensitivity of the camera or distortions in the optical path.

Additional figures

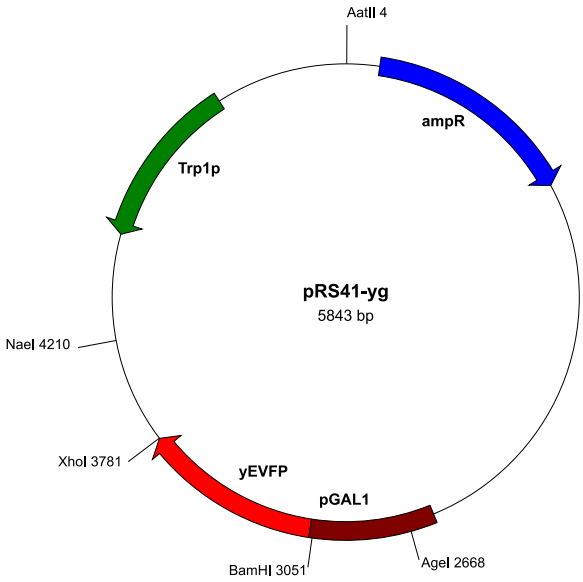

Figure S8: Map of the pRS41-yg vector used to integrate 3 copies of the GAL1 promoter driving expression of yeast-enhanced Venus fluorescent protein into the yeast genome. The vector was constructed using standard recombination techniques from two commercially available vectors: the tryptophan marker from pRS404 was inserted into the pESC-His vector, which contains the GAL1-10 promoter locus of *S. cerevisiae*, by cutting both vectors at the AatII and NaeI restriction sites. The yeast-enhanced Venus fluorescent protein (yEVFP), a YFP variant, was inserted downstream of the GAL1 promoter into the BamHI and XhoI restriction sites. To prepare for yeast transformations, the resulting vector, pRS41-yg, was cut at the AgeI restriction site within the GAL1-10 promoter locus, to ensure sufficient homology for recombination into the yeast genome.

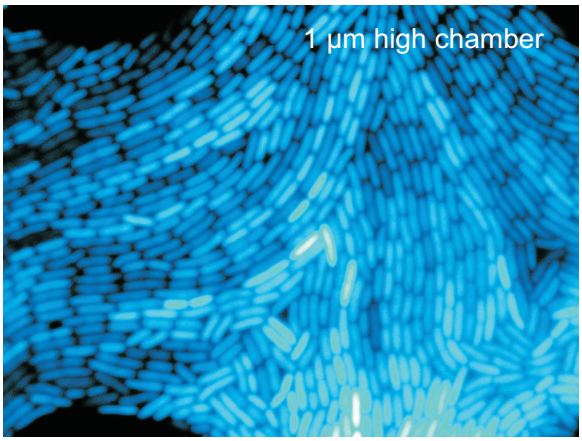

Figure S9: The TμC device can be customized for different cell types: a 1 μm high *E. coli* trapping microchemostat full of cells after ∼12 hours of growth. Empty ovals in the trapping region are posts required to support the low height.

References

[1] Cowen, E. A. & Sveen, J. K. *PIV and Water Waves*, chap. Chapter 1: Quantitative imaging techniques and their application to wavy flows, 1–49 (World Scientific, 2003).

[2] Haberman, R. *Elementary applied partial differential equations: with Fourier series and boundary value problems* (Prentice Hall, Upper Saddle River, NJ, 1998), 3rd edn.

[3] Bird, R. B., Stewart, W. E. & Lightfoot, E. N. *Transport phenomena* (John Wiley & Sons, New York, NY, 1960), 1st edn.

[4] Venturoli, D. & Rippe, B. Ficoll and dextran vs. globular proteins as probes for testing glomerular permselectivity: effects of molecular size, shape, charge, and deformability. *Am J Physiol Renal Physiol* **288**, F605–613 (2005).

[5] Adams, R. & Bischof, L. Seeded region growing. *IEEE Transactions on Pattern Analysis and Machine Intelligence* **16**, 641–7 (1994).

[6] Vincent, L. Morphological grayscale reconstruction in image analysis: applications and efficient algorithms. *IEEE Transactions on Image Processing* **2**, 176–201 (1993).

[7] Crocker, J. C. & Grier, D. G. Methods of digital video microscopy for colloidal studies. *Journal of Colloid and Interface Science* **179**, 298–310 (1996). See also "Particle tracking using IDL" online tutorial developed by E. Weeks, http://www.physics.emory.edu/ weeks/idl/.